NANO · MICRO small
www.small-journal.com

Dislocation-Free and Atomically Flat GaN Hexagonal Microprisms for Device Applications

Maryam Khalilian, Zhaoxia Bi, Jonas Johansson, Filip Lenrick, Olof Hultin, Jovana Colvin, Rainer Timm, Reine Wallenberg, Jonas Ohlsson, Mats-Erik Pistol, Anders Gustafsson, and Lars Samuelson**

III-nitrides are considered the material of choice for light-emitting diodes (LEDs) and lasers in the visible to ultraviolet spectral range. The development is hampered by lattice and thermal mismatch between the nitride layers and the growth substrate leading to high dislocation densities. In order to overcome the issue, efforts have gone into selected area growth of nanowires (NWs), using their small footprint in the substrate to grow virtually dislocation-free material. Their geometry is defined by six tall side-facets and a pointed tip which limits the design of optoelectronic devices. Growth of dislocation-free and atomically smooth 3D hexagonal GaN micro-prisms with a flat, micrometer-sized top-surface is presented. These self-forming structures are suitable for optical devices such as low-loss optical cavities for high-efficiency LEDs. The structures are made by annealing GaN NWs with a thick radial shell, reforming them into hexagonal flat-top prisms with six equivalents either m- or s-facets depending on the initial heights of the top pyramid and m-facets of the NWs. This shape is kinetically controlled and the reformation can be explained with a phenomenological model based on Wulff construction that have been developed. It is expected that the results will inspire further research into micron-sized III-nitride-based devices.

1. Introduction

During the last two decades, III-nitrides have emerged as one of the dominating material systems for semiconductor-based light sources in the green to ultraviolet (UV) spectral range and a variety of lasers based on III-nitrides have been demonstrated.[1–11] Device design has been hampered by material constraints, arising from the lattice mismatch of either the epitaxial layer/growth substrate, or the heteroepitaxy of layers, leading to the introduction of a high density of dislocations. The high dislocation density increases the nonradiative recombination rate and reduces device lifetimes.[12–14] It also increases lasing thresholds for laser diodes. Despite the high dislocation density, highly efficient nitride-based optical devices have been successfully manufactured. Significant research efforts have been focused on overcoming the issues of dislocations and

Dr. M. Khalilian,[+] Dr. Z. Bi, Prof. J. Johansson, Dr. O. Hultin,[++] Dr. J. Ohlsson,[+++] Prof. M.-E. Pistol, Prof. A. Gustafsson, Prof. L. Samuelson
Solid State Physics and NanoLund
Lund University
Box 118, Lund 221 00, Sweden
E-mail: Maryam.khalilian@gu.se; lars.samuelson@ftf.lth.se

The ORCID identification number(s) for the author(s) of this article can be found under https://doi.org/10.1002/smll.201907364.

[+]Present address: Department of Physics, University of Gothenburg, SE412 96 Göteborg, Sweden
[++]Present address: RISE Research Institutes of Sweden AB, Scheelevägen 17, 223 70 Lund, Sweden
[+++]Present address: Hexagem AB, Scheelevägen 15, Ideon Alpha 3, 223 63 Lund, Sweden
[++++]Present address: Division of Production and Materials Engineering, Department of Mechanical Engineering, Lund University, Box 118, 221 00 Lund, Sweden

DOI: 10.1002/smll.201907364

Dr. F. Lenrick,[++++] Prof. R. Wallenberg
nCHREM/Centre for Analysis and Synthesis and NanoLund
Lund University
Box 124, Lund 221 00, Sweden
Dr. J. Colvin,[+++] Prof. R. Timm
Synchrotron Radiation Research and NanoLund
Lund University
Box 118, Lund 221 00, Sweden

strain. For example, a 25% lower threshold energy density of electrically injected UVC edge-emitting lasers[14] was achieved by replacing the epitaxially laterally overgrown AlN/sapphire substrates with low defect-density AlN substrates. The reduction in the threshold was attributed to a reduced dislocation density by two orders of magnitude. However, it is virtually impossible to grow dislocation-free III-nitrides using conventional epitaxial growth techniques based on film growth on lattice-mismatched substrates such as GaN-on-sapphire.[15–17]

To overcome the epitaxial challenges of film growth, one of the most promising methods is 3D growth.[18–20] An example is device structures based on nanowires (NWs) with subsequent overgrowth by radial layers. GaN-on-sapphire (or GaN-on-Si and GaN-on-SiC) substrates typically have a threading dislocation (TD) density in the range of 10^7–10^9 cm^{-2}. Due to their small footprint on the substrate, NW growth can virtually eliminate the propagation of the TDs, even when grown on substrates with a high density of TDs. This has previously been reported by many groups.[21–27] The 3D NW geometry can accommodate 5–10 times higher coherent strain than similar planar structures.[28] However, a challenge of 3D growth is to control the growth rates on the different crystal facets defining the structures. The growth rates depend on the V/III ratio, growth temperature, and type of carrier gas.[29–31] Under typical growth conditions used to grow III-nitride NWs on (0001)-oriented substrates, the fastest-growing crystal facet, the top c-facet, will disappear, and the final shape of the structure is defined by the slowest-growing facets, normally the s- and m-facets. These facets are indicated in **Figure 1**. The typical NW shape consists of a hexagonal pillar with six m-facets, and a hexagonal pyramid tip defined by six s-facets.[29,32] This geometry limits the design of optoelectronic devices, as the pointed tip causes optical losses in optical cavities due to scattering, preventing the formation of high-quality vertical resonators. It also results in device fabrication complexities. Another group of devices affected by dislocations is transistors, especially high electron mobility transistors.

In this paper, we demonstrate a novel growth method to achieve dislocation-free GaN prisms with atomically smooth sub-micrometer-sized c-facets which can offer a solution for the fabrication of high quality optoelectronic devices, for example, vertical-cavity surface-emitting lasers with low threshold currents. The method we have developed for the growth, relies on the use of selected area growth in combination with a pre-growth thermal annealing of the substrate to filter out TDs from the substrate. The growth is initiated with the growth of NWs followed by the growth of a thick radial layer, resulting in a structure with a hexagonal pyramid on top of a hexagonal prism. After the NW growth, the sample is annealed in situ in order to reform the shape into an equilibrium shape hexagonal prism with a nearly atomically smooth surface. These prisms are dislocation free, confirmed by a combination of transmission electron microscope (TEM) studies on how the dislocations affect the shape, corroborated by atomic force microscopy (AFM). Scanning electron microscopy (SEM) is then used to identify the structures containing dislocations. The absence of dislocations is confirmed independently by cathodoluminescence (CL) imaging.

2. Result and Discussion

2.1. Growth of GaN Hexagonal Microprisms

The growth of dislocation free microprisms relies on two crucial steps. Masking off most of the surface of the substrates with only small holes to grow from, blocks most of the TDs from the substrate. Combining this with thermal annealing to prepare the surface in the hole to bend the TD in the hole before they propagate out of the hole. This ensures that the majority of the structures grown from the holes are dislocation free. By employing different growth conditions, we make a structure with hexagonal pyramid on top of a hexagonal prism. By thermal annealing, we transform this into a hexagonal prism with a flat top. As the starting material is dislocation free, the resulting prisms are also dislocation free.

The epitaxial growth method used in this paper is illustrated in Figure 1 by schematics (in blue) and SEM images. Before the epitaxial growth, the (0001)-oriented GaN-on-sapphire substrate is covered by a dielectric SiN_x mask with holes, 60 nm in diameter, for the selective area growth of the NWs, as described in more detail in the method section. The patterned substrate is annealed in the metal-organic chemical vapor deposition (MOCVD) reactor to precondition the flat GaN buffer layer in the holes before the NW growth, as well as to ensure a clean GaN surface. The first growth step is to fill the holes (nucleation step) and to proceed with the NW growth, as shown in Figure 1a. With the growth conditions commonly used for NW growth, the growth rate of the m-facets is negligible compared with the growth rates of the other crystal facets. At this stage, the NW is a long hexagonal pillar with a small hexagonal pyramid on top.

This first step lays to foundation for eliminating dislocations from the final structure. The main contribution is a purely mechanical feature of the mask. By only growing through the holes in a mask with a low hole-to-mask density, most of the TDs are stopped by the mask. As an example, with a hole diameter of 100 nm and the areal density is about 1 hole μm^{-2}, and the holes cover about 1% of the surface. With a dislocation density of 10^8 cm^{-2}, or 1 μm^{-2}, the chance of one hole containing a dislocation is about one in 100. A further reduction of the diameter to 50 nm would reduce the probability to a quarter, or one in 400. It is important that the hole size is smaller than the average TD density. This allows us to use substrates with a high density of TDs for the growth. Masking alone does not ensure the growth of dislocation free structures. It is also important to include an annealing step before the NW growth. The annealing leads to etching of the surface under the hole to transform the c-facet to a V-shaped pit. The role of their inclined planes in bending the few dislocations in the hole is discussed in the Supporting Information. This will make sure that than virtually no dislocations propagate through the holes in the mask, but are bent to the sides of the holes and therefore eliminated from the NWs. Without this step, we also observe generation of additional TDs during the NW nucleation. A more detailed discussion of the two filtering mechanisms is given in the Supporting Information.

The radial growth of GaN on the NW can be enhanced by increasing the growth rate of the m-facets relative that of the

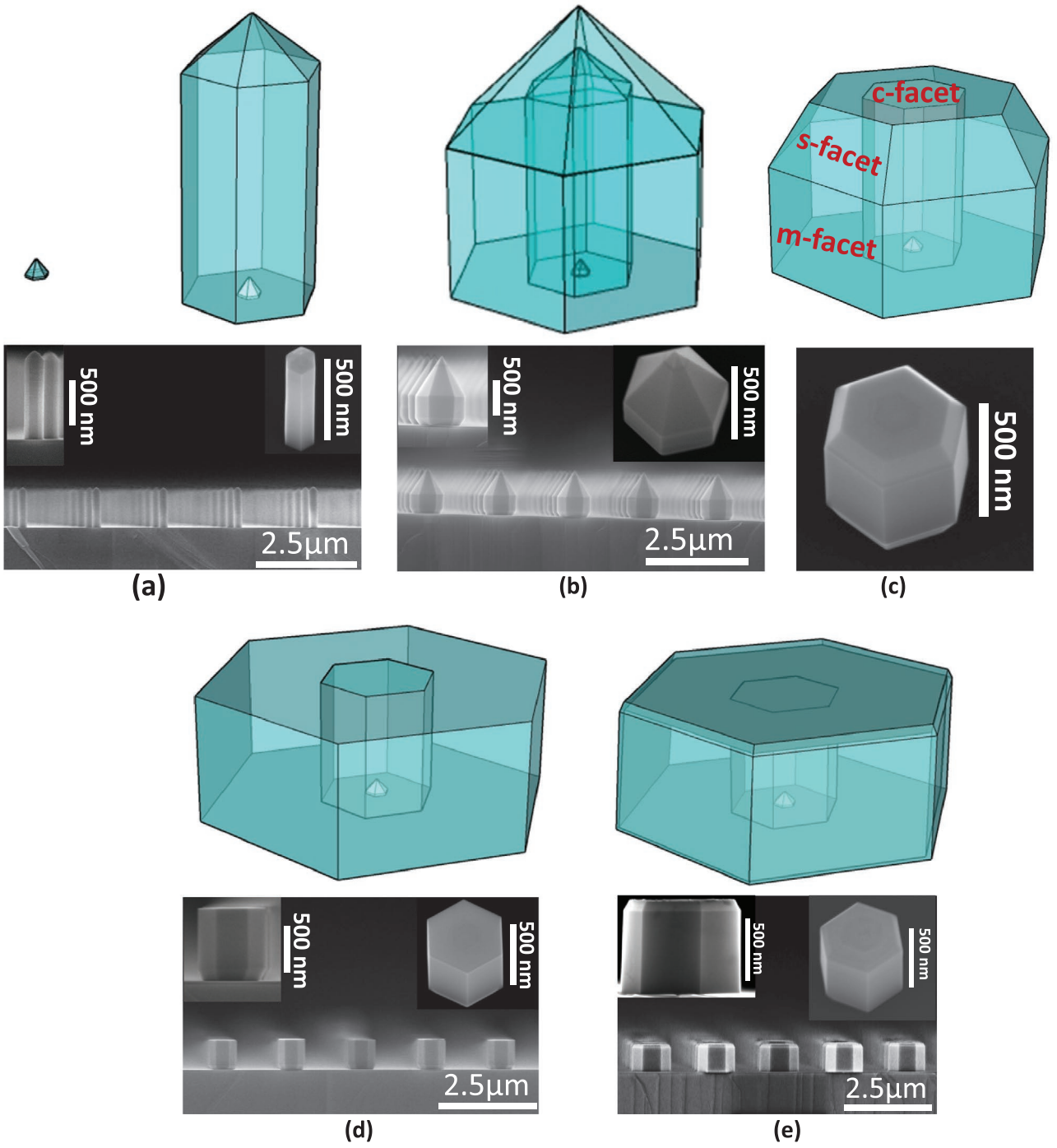

Figure 1. Schematics and SEM images of the growth sequence. a) Nucleation and NW growth on an array of holes in a SiN_x mask. b) Radial growth of GaN used to control the size of the final structure. c,d) Time evolution of the reformation of the structure in (b) into a hexagonal GaN prism with a flat-top c-oriented surface. e) Epitaxially grown GaN layer on the flat-top GaN prism used to ensure a smooth top c-facet. The insets of the low-magnification SEM images are side-view and 30° tilted-view images of single structures. The crystal facets (c: (0001), m: $\{10\bar{1}0\}$ and s: $\{10\bar{1}1\}$) are indicated in schematic image of (c).

s- and c-facets.[33,34] We achieved this by changing the growth parameters to promote the growth of pyramid-shaped GaN structures. The s-facets will evolve and eventually dominate the shape of the structure as shown in Figure 1b. The observed shape is consistent with the kinetic Wulff construction, as reported by Jindal and Shahedipour–Sandvik.[33] They reported a full hexagonal pyramid shape defined by s-facets as the final shape and a truncated hexagonal pyramid (with a flat c-facet) as the transient shape for selective area growth of GaN. With a long enough radial growth time, our structure will take the shape

of a full hexagonal pyramid defined by only s-facets. However, the growth time of the radial layer can be controlled to obtain the desired structure, typically a hexagonal pyramid on top of a hexagonal prism, as shown in Figure 1b. This radial growth step allows us to tune the height-to-width ratio of the NWs and thereby determine the volume and dimension of the flat-top GaN prism resulting from the subsequent step, the in situ reformation step. Figure 1c,d shows the time evolution of the reformation step, in which the c-facet is restored and the s-facets are eliminated. A similar approach has been used to reshape InN NWs in order to flatten the side facets as an intermediate step, where the resulting structure is defined by m- and c-facets.[35] The reformation is discussed in more details in Section 2.3.

The final step, shown in Figure 1e, is an epitaxial GaN-layer (with a thickness on the c-facet of ≈80 nm) grown on the flat-top GaN prism to achieve an atomically flat c-facet. This smooth surface is essential for device applications. For example, in a vertical-cavity laser, the smooth surface minimizes optical scattering losses, to achieve low-loss cavities. Using a more dense array of NWs, it is possible to create a solid GaN film by merging the individual prisms during the reformation, as described in ref. [36].

2.2. Structural Characterizations of Dislocation-Free and Atomically Flat GaN Prisms

The structural properties of the GaN prisms have been studied by SEM, as presented in Figure 1 and in the Supporting Information. We have studied the evolution of the shape of the structure from the seeding NW to the final shape of the prism. Apart from the shape and homogeneity of the structures, we have developed a technique to identify prisms and NWs that contain dislocations using SEM imaging. From a combined study of SEM and TEM imaging, we have identified that the all structures that contain one or more dislocations have an asymmetric shape. From the TEM study, it is clear that the asymmetry stems from dislocations that go through the hole in the mask and propagate into the seed nanowire. Near the mask, they tend to bend toward one of the side facets. The dislocation induces a higher growth rate on this facet, which leads to an asymmetric shape, like in **Figure 2**c. It is therefore simple to identify the structures containing dislocations in top view SEM imaging. The technique is described in detail in the Supporting Information. The TEM studies were performed on thin lamellae produced by focused ion beam milling (FIB). Different TEM techniques were used to study the prisms to reveal different features. High-resolution (HR) TEM imaging was used to study the crystalline quality and low-angle annular dark field (LAADF) was used to identify the presence of dislocations in the substrate and grown structures. The TEM images were recorded in the $\langle \bar{1}\bar{1}20 \rangle$ zone axis. Figure 2a shows a typical LAADF image of the structure in Figure 1e, with a corresponding HRTEM image in Figure 2b. The inset in Figure 2a shows an electron diffraction pattern, confirming that the GaN structure is single crystalline. The crystal structure shows no stacking faults in the HRTEM images, indicating a perfect GaN crystal structure. Although TDs are clearly visible as bright lines in the GaN buffer layer in LAADF images, we do not observe any dislocations in the prisms grown with the initial annealing step. Figure 2c shows a LAADF image of a prism grown without the initial annealing step. A TD penetrates the hole in the mask and continues into the prism. Just above the mask, the dislocation bends to the left in the image. The dislocation causes an increased growth rate on that particular facet, leading to an asymmetric shape of the prism. This asymmetry can be used to identify prisms and nanowires containing dislocations, as discussed in detail in the Supporting Information. Though the thin lamellae only sample a portion of the structures as they need to be electron transparent, they still reveal all dislocations. In all our TEM studies, we have never encountered any generation of dislocations inside the structures. As all TEM images include the hole, any dislocation bending out of the lamellae would still be partially visible above the mask.

Further structural characterization was performed using AFM. **Figure 3**a–c shows a comparison between AFM images of a thin epitaxially grown GaN layer on a GaN-on-sapphire substrate and on a GaN prism, both grown under the same conditions, to the same thickness (30 nm). In contrast to the c-facet on the GaN prisms, the planar GaN shows defect-related pits. Pits and hillocks are typically associated with the termination of TDs on the surface.[36–38] The absence of pits and hillocks on the top facet of the prism supports the conclusions from the TEM images of dislocation-free GaN prisms. The root-mean-square (RMS) surface roughness of the two samples was compared. The RMS of the planar surface sample is 0.6 nm over a

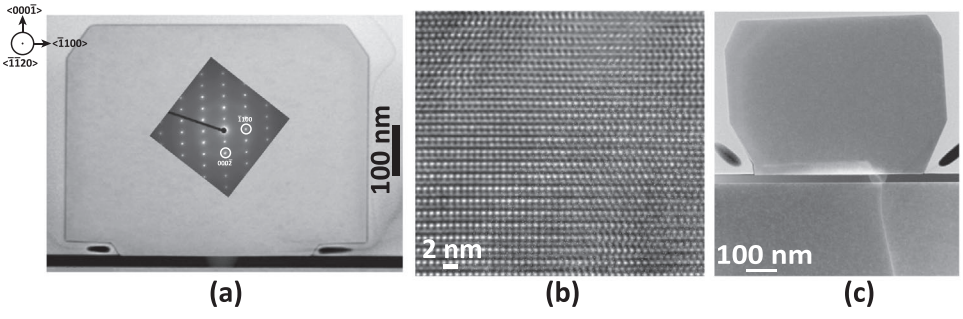

Figure 2. TEM images of an epitaxial layer of GaN grown on a GaN prism, similar to the one in Figure 1e. a) LAADF-TEM image and b) HRTEM image of a flat-top GaN prism. The inset in a) shows the corresponding electron diffraction pattern. Panel (c) shows an LAADF-TEM image of a prism where a dislocation (bright line contrast) penetrates from the substrate, through the hole in the mask, the dislocation bends just above the mask toward the sidewall.

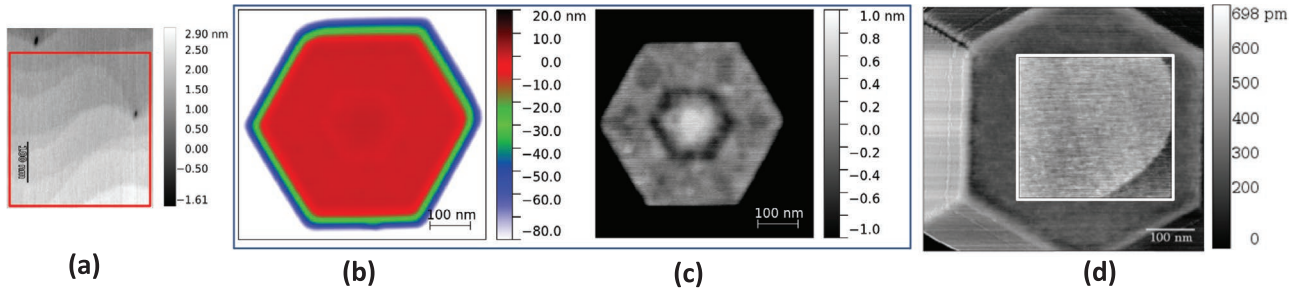

Figure 3. AFM topography images of a) a planar epitaxial layer of GaN grown on a GaN buffer layer and b,c) an epitaxial layer of GaN grown on a flat-top GaN prism, both have the same thickness and been grown under the same growth conditions. Note that both images in (b) and (c) show the same area, but using different height ranges. d) The top facet of a prism with an 80 nm GaN top layer showing a single bilayer step.

$0.4 \times 0.4\ \mu m^2$ scan size (both with and without the inclusion of the defects), while the flat-top GaN prism has an RMS surface roughness of 0.3 nm over the entire flat-top c-facet surface, corresponding to a similar scan size. The AFM image in Figure 3c also reveals variation on a bilayer scale especially around the central NW for the flat-top GaN prism with a thin epitaxial GaN-layer.

A GaN-layer with a thickness of 60 nm or more yields an almost atomically flat GaN surface, as shown in Figure 3d. However, the growth of an epitaxial layer of GaN on the prism reintroduces the s-facets; as a result, the thickness of this layer should be optimized for different device applications.

2.3. Reformation of the Nanowires and the Wulff Model

Unlike conventional MOCVD growth, which is performed far from equilibrium conditions, for the reformation step, the group III precursor is turned off and the shape of the structure is allowed to reach equilibrium. Due to the near equilibrium condition, the crystal reformation is a spontaneous mechanism whereby crystal facets with a high surface energy are reduced in size in favor of facets with a low surface energy. This can be understood in terms of the equilibrium shape Wulff model, which predicts the shape of a crystal based on the relative surface energies of the facets.[33] Consequently, the basic kinetical parameters of crystal growth, the activation energies of atomic incorporation (into the crystal) and atomic dissociation (from the crystal), vary with the surface energy of the facets. These two mechanisms govern the crystal shape-transformation. During this reformation-step, no additional Ga is supplied but the crystal Ga is recycled. The Ga-atoms dissociated from the crystal facets accumulate in a surface-bound phase, capable of a high atomic density and a high surface mobility. Though molecular beam epitaxy uses totally different growth conditions, this behavior was observed during annealing.[39,40] In order to achieve a high density of mobile and surface-bound Ga atoms, the desorption rate of atomic Ga to the gas phase must be low and the atomic diffusion length must be high relative the size of the facets. This requirement is clearly fulfilled as the GaN-crystal volume remains essentially constant before and after the reformation as the shape is modified.

The equilibrium Wulff construction[41] can be used to explain the shape[33] of the reformed structure. The possible facets defining the shape of the prisms are a, c, m, and s. Using the surface energies from ref. [33] ($\gamma_a = 159$ meV Å^{-2}, $\gamma_m = 137$ meV Å^{-2}, $\gamma_c = 129$ meV Å^{-2}, and $\gamma_s = 181$ meV Å^{-2}), the equilibrium prism should be defined by m- and c-facets, with a height-to-width ratio of $\gamma_c\sqrt{3}/(2\gamma_m) \approx 0.82$, where the width is defined as the long diagonal (corner or corner) of the hexagonal prism.

The small s-facet we observe at the base of the prism (see Figure 1d) can be caused by slightly lower value of γ_s at the bottom, in the vicinity of mask. The shape we observed is a hexagonal prism with a height-to-width ratio of about 0.81 and small s-facet at the bottom, see Figure 1 and **Figure 4**. This clearly implies that equilibrium is reached during the reformation process.

During the reformation step, the shape gradually approaches the equilibrium shape. However, the reformation is also governed by geometric constraints and surface diffusion kinetics. According to our observations, the base area of the structure never shrinks during reformation. A likely reason for this is a reduced mobility of the atoms at the bottom interface which is in contact with (or in close proximity to) the mask. In addition, a minimum initial height of the vertical m-facets is required for the equilibrium structure (the m- and c-facet bounded prism described above) to form.

Based on our observations, we propose a phenomenological model for the reformation, driven by a reduction of the total surface energy in combination with the available material. The starting point of our model is limited to our starting point, which is a pyramid, consisting of s-facets, on top of a hexagonal prism, defined by m-facets. Depending on the height of the m-facets with respect to the height of the pyramid, there are two final outcomes, either a fully hexagonal prism, defined by m- and c-facets, or a truncated pyramid defined by s- and c-facets. It is worth pointing out that the width and height of the initial NW is of no importance, as it is the shape and dimensions of the structure to reform governs the outcome. In order to reduce the surface energy, the area of the s-facet must be reduced in favor of the c- and m-facets. Material from the top of the pyramid (the part of the structure bounded by s- and possibly c-facets) is released and diffuses down along the s-facet. The material incorporates into the s- and m-facets, thereby reestablishing a top c-facet. The process is illustrated Figure S5 (Supporting Information). It is reasonable to assume that the edge between the s- and m-facets acts as a barrier for surface diffusion, which explains why only a certain fraction of the material from the tip reaches and incorporates into the m-facets. Figure 4 shows the shape limits, as a function of the fraction

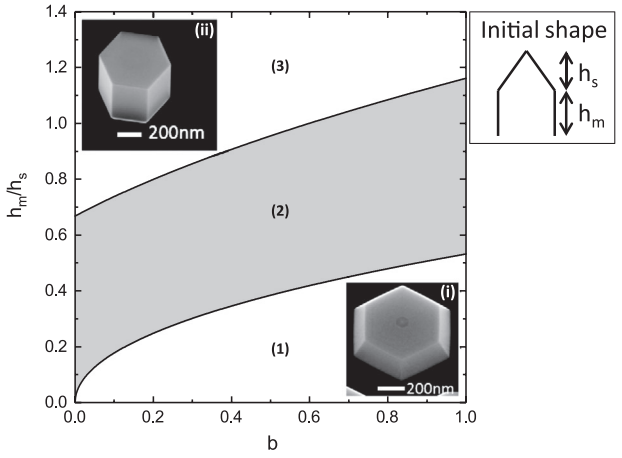

Figure 4. Shape transformation during the reformation step as a function of material from the tip region (the part of the structure bounded by s-facets) that redistribute and incorporate at the m-facets. h_m/h_s defines the height ratio between m- and s-facets, as shown schematically in the inset, and b corresponds to the fraction of material from the tip region (the part of the initial structure limited by s-facets) that incorporates into the m-facet. If h_m/h_s is below the gray area (region 1), the reformation step results in a structure with flat-top c-facet bounded with six equivalent s-facets, as shown by the inset SEM image (i). The gray area (region 2) indicates an intermediate stage where it is possible to reshape into a structure with smaller height to width ratio than the equilibrium structure. Finally, if h_m/h_s is above the gray area (region 3), the structure can reform into the fully equilibrated structure, a structure with flat-top c-facet surrounded with six equivalent m-facets, as shown by the SEM image inset (ii).

of tip material, b, that crosses the barrier between the s- and m-facets and incorporates into the m-facets. b = 0 means that no material is incorporated into the m-facet and the base are is conserved. The initial shape is given by h_m/h_s, where h_m and h_s are the heights of the m-facets and the top pyramid before reformation in the c-direction, see the schematic in Figure 4. The figure identifies three different regions of height ratios. If the initial ratio of h_m/h_s is low (region 1), the diffusing material will be incorporated on the m-facet, transforming it into an s-facet. Though the side facets are high-energy s-facets, the total energy has been reduced, as the area of c-facets has increased. Any further reshaping would extend the s-facets, leading to a wider and flatter structure, and the reshaping results in flat s- and c-facet bounded structures, see inset (i) in Figure 4. With a higher initial value for h_m/h_s (region 2), the amount of material diffusing from the tip is not enough to make the m-facets vanish completely. The diffusion barrier between the m- and s-facets still exists and the material that remains at the tip can now reshape and deposit on the s-facets, effectively increasing the m-facet height and c-facet area, while decreasing the s-facet area. Finally, for a sufficiently high h_m/h_s ratio (region 3), the m-facets developed after redistribution of material from the tip, which leads to the formation the equilibrium, hexagonal prism structure, see inset (ii) in Figure 4.

In region 2, the reformation still leads to structures bounded by m- and c- facets (and potentially also remaining s-facets), but having a smaller height-to-width ratio than the fully equilibrated structures. It is important to stress that these structures cannot equilibrate because the base areas never shrink and their base areas are too wide in relation to the accessible amount of material. We also stress that the fraction b probably depends strongly on experimental conditions, especially temperature, but potentially also the size. Therefore, only one b-value is relevant for a certain set of experiments carried out under similar conditions. A quantification of b has limited relevance due to the qualitative features of the model. One conclusion that can be drawn is that with the constraint that the base area cannot shrink, it is impossible to reform a full pyramid into a hexagonal prism. From the plot, we obtain the minimum h_m/h_s ratio that can be reformed into the equilibrium shape of about 0.67, for $b = 0$.

For all the prisms in this study that are reformed to be defined by only c-and m-facets, where the s-facets are removed, we find a height-to-width ratio ranging from 0.64 to 1.14. From the discussion and model above, we can conclude that a ratio after the reformation below the equilibrium value of 0.82 is most likely in region 2, where there is not enough material to reach the equilibrium shape, under the constraint above that the bottom area cannot shrink, but the prism is still defined by c- and m-facets. If on the other hand, the ratio is larger than 0.82, the equilibrium shape has not been reached. Most likely, the reformation has not been given enough time to establish the equilibrium shape. Once the high-energy s-facets are consumed, the reformation slows down. The driving force behind the continued reformation is the 6% difference in surface energy of the c- and m-facets, as discussed above. This should be compared with the 14 and 25% difference between the s-facet and the m- and c-facets. The reformation of a prism defined by c- and m-facets to the equilibrium shape takes much longer time. It is therefore essential to control the height of the initial NW and the width of the radial layer to avoid a very long reformation time.

The objective of this project is not only to grow prisms with a perfect shape, but also to grow them dislocation free. To identify the presence of dislocations in individual structures is often time consuming with limited statistics, like the LAADF imaging used in the present paper. In order to study the presence of the dislocations in our structures, a faster approach with more reliable statistics is need. In Section S1 in the Supporting Information, we present an SEM-based approach we have developed to identify structures that contain dislocations. Furthermore, to grow dislocation-free structures, the effect of the thermal annealing of mask opening before the growth (Section S2, Supporting Information), diameter of mask opening (Section S3, Supporting Information), and growth conditions have been investigated. The data show that to grow dislocation-free NWs and prisms, both a small enough hole diameter and a pregrowth thermal annealing step must be used as one of these conditions alone is not sufficient to eliminate the dislocations. However, the NW growth conditions did not seem to influence the blocking of the TDs. This is expected, as the filtering has already taken place when the NWs form.

2.4. Optical Characterization

In order to get an independent assessment of the quality of the reformed structures, we have performed spatially and spectrally and resolved CL studies. CL is an excellent tool to probe optical

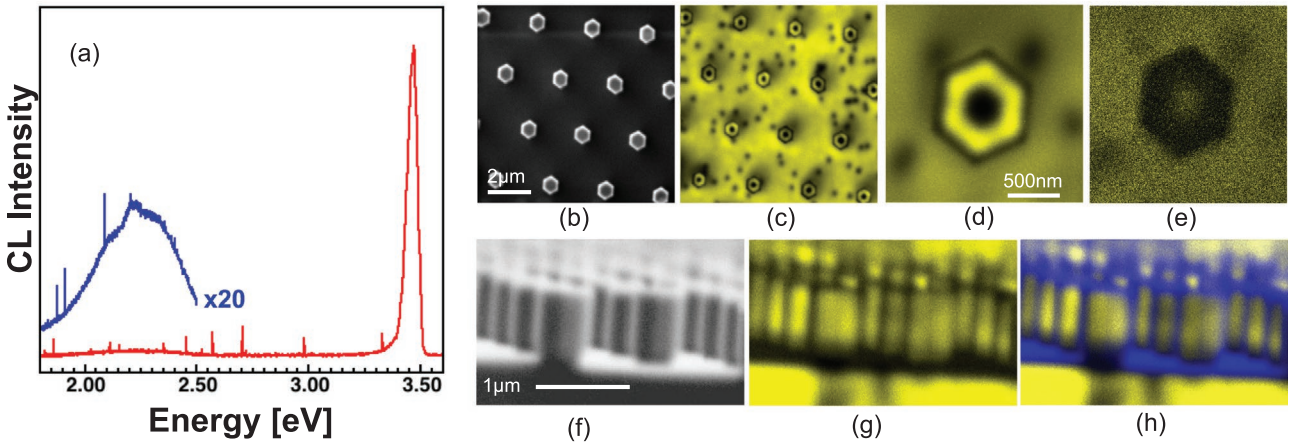

Figure 5. Top- and side-view CL imaging. Panel (a) shows an average spectrum. Panel (b) shows a top view SEM image and (c) shows the corresponding monochromatic CL image of an area with prisms using the NBE emission and (b) shows the corresponding top view SEM image. Panels (c)–(e) show monochromatic CL images of a single prism using the NBE (d) and YLE (e). Panel (f) shows an SEM cross-sectional view of the same structure and (g) the corresponding NBE CL image. Panel (h) shows a color composite image, combining the SEM (blue) and CL (yellow) images.

properties of semiconductors, especially suited to high bandgap materials like GaN. Not only can it map the local variations of different emission centers, but also the absence of emission. As most dislocations in GaN introduce nonradiative recombination, they can easily be identified as dark spots and dark lines, depending on their geometry.[42] We are therefore able to study large numbers of structures in a limited time and without any sample preparation. Examples of the effect of dislocations are shown in Figure S2 (Supporting Information). TDs from the substrate beside the structures are visible as dark spots, and a dislocation in a structure shows significantly reduce emission intensity, locally.

Figure 5 shows an average spectrum and a series of images. Figure 5a shows a typical low-temperature CL spectrum, showing near bandgap emission (NBE) and yellow band emission (YLE). Figure 5b shows a top view SEM image and Figure 5c a CL image, recorded using the NBE. Figure 5e,f shows a single prism at higher magnification, using the NBE (e) and YLE (f). The dark spots in the area between the prims in Figure 5c are caused by TDs ending at the GaN-substrate surface, as the dislocations introduce nonradiative recombination. In contrast, no dark spots associated with dislocations have been observed in the GaN prisms. The dark center of each prism is related to the original GaN seed NW, which has dominating yellow band emission.[43,44] This is clear from the CL images of a single prism, as shown in Figure 5e,f. The NBE emission leaves a dark spot in the center, which is filled in by the yellow band emission. Neither of these images show any dark spots or lines of dislocations. It should be pointed out that the dark lines at the edges of the prisms are commonly observed in for example NWs due to a higher escape probability of the electrons from the structure at edges and thereby a lower excitation probability of the material at these locations.[45] Figure 5f shows an SEM side view of a cleaved sample and Figure 5g the CL image recorded at the same time using the NBE. To help identifying the side facets of the prisms, we have included a color composite image (h), combining the CL (yellow) and the SEM (blue) images. The emission is uniform along the prism, from bottom to top, indicating a homogenous material quality. We observe the same reduction in intensity of the emission at the corners of the prisms. In addition, there are dark lines where at the edges of the prisms, where the top prism shadows the one behind it. The substrate surface also appears dark, as this surface faces away from the detection system. The clearest indication that the prisms are dislocation free is to follow the intensity along the individual facets. The CL imaging further supports the fact that the GaN prisms are dislocation-free. Using CL imaging, we can investigate large areas and many prisms in a relatively short timeframe, especially when compared with the time consuming TEM characterization. The data shown in Figure 5 show shows the absence of dislocations in the prisms. The Supporting Information includes a comparison of a symmetric and an asymmetric prism, where the asymmetric prism exhibits a reduced emission intensity in the direction of the extended facet containing a dislocation (see Figure S5 in the Supporting Information).

3. Conclusion

In this paper, a novel growth technique is presented to address current material-related challenges of III-Nitride-based optical devices by the growth of dislocation-free and atomically flat sub-micrometer-sized hexagonal GaN prisms. The method is based on two distinctly different epitaxial steps with different energy minimization mechanisms: 1) NW growth in combination with thermal annealing of the substrate, allowing for the filtering of TDs. 2) Crystal reformation to re-establish a dominant c-facet surrounded by six equivalent m- or s-facets. To the best of our knowledge, this is the first report on the complete elimination of TDs, combined with the creation of an atomically flat, sub-micrometer-sized GaN structure. Our approach has resulted in the development of a new growth technique in order to shape GaN nanostructures in a 3D growth mode. It is quite striking how equilibrium-based self-assembly of the material structures results in a perfect, atomically smooth hexagonal

prism, identified as an ideal cavity structure for optical devices. Our results show that dislocation-free and flat-top GaN prisms, which have the potential to accommodate large lattice-mismatch, can pave the way for a new generation of small footprint devices, such as highly efficient lasers and light-emitting diodes in the range from red to deep UV, solar blind photodetectors and even extending into high electron mobility devices. To further prove the benefit of the GaN microprism, vertical optical cavities based on these structures have been designed and fabricated. We have embedded them between two dielectric Bragg mirrors to obtain electron beam pumped optical cavities. The data show the presence of one single longitudinal mode which proves that dislocation-free and flat-top GaN prisms have the potential to develop new generation of lasers. This data will be presented elsewhere.

4. Experimental Section

Growth—Pretreatment and Preparation of the Growth Substrate: In these experiments, a commercial 2″ (0001) GaN buffer layer grown on sapphire substrate was used as starting point. The epitaxial GaN layers on these wafers comprise a 2 µm n-doped GaN ($n = 10^{18}$ cm^{-3}, and a TD density of 10^8 cm^{-2}) layer on top of 2 µm thick undoped GaN. A 30 nm thick dielectric mask made of SiN_x was deposited and patterned with arrays of nanosized holes by electron beam lithography and reactive ion etching. The diameters of the holes were 50–100 nm for the dislocation filtering investigation. The optimized diameter for the growth of hexagonal prisms was 60 nm. The wafer was diced into 8×10 mm^2 pieces and cleaning steps were performed before and after the dicing. The growth was performed in one sequential growth run in a Thomas Swan close coupled showerhead MOCVD reactor. The material sources used were TEG and NH_3.

Growth—First Epitaxial Step: NW Growth (Figure 1a): Before growth, the substrate was cleaned, in situ, by an annealing step with an NH_3 background flow of 3 l min^{-1}, using a mixture of N_2 and H_2, and at a 150 °C higher temperature compared with the NW growth temperature. After this step, NWs were grown with a V/III ratio of 7.69 and at the growth temperature of 930 °C and its growth rate was 24×10^{-5} µm^3 s^{-1} and the growth time was 5 min.

Growth—Second Epitaxial Step: Radial Shell Growth (Figure 1b): For this step, the growth parameters were chosen to enhance radial growth. Typically, the radial growth took place at 880 °C, with a V/III ratio of 20 500, using only N_2 as the carrier gas. The growth time was 38 min.

Growth—Third EPITAXIAL Step: Reformation (Figure 1c,d): The reformation was performed at an elevated temperature (1000 °C) in the presence of NH_3 (9.5 l min^{-1}) but without the Ga source and N_2 as the carrier gas. The structure was reformed for 60 min.

Growth—Fourth Epitaxial Step: A Layer of GaN on the Flat-Top GaN Prism (Figure 1e): In the last step, an epitaxial layer of GaN was grown on the flat-top GaN prism to smoothen the surface. This step used the same growth conditions as the second step and the growth time was around 8 min, depending on the intended thickness of this layer.

Transmission and Scanning Electron Microscopy: All of the grown samples were characterized by SEM images in top, 30° tilted, and side view, using Hitachi SU8010 cold field emission SEM setup operated at 10 kV. For cross-sectional scanning TEM (STEM) and TEM studies, the sample preparation was done in several steps by focused ion beam (FIB) to make thin specimens transparent to electrons. In order to extract a thin section of the sample, typically five prisms were covered by a thin layer of electron-beam-induced deposition of Pt followed by a thicker, second Pt layer deposited by ion beam, where the first layer was deposited to prevent further damages caused by the ion beam. Next, a lamella was removed from the native substrate by FIB etching, lifting out by an OmniProbe and transferring to a Cu half grid. Finally, the lamella was thinned down by polishing it from both sides with the ion beam until the thickness of about 100 nm was achieved. The FIB milling was performed using an FEI Nova NanoLab 600 dual beam FIB/SEM equipped with an OmniProbe micromanipulator. TEM characterization was performed using a field-emission TEM/STEM (JEOL 3000F at 300 kV) with an Oxford Instruments XEDS detector and an annular dark-field detector.

Atomic Force Microscopy: AFM measurements were performed using a Bruker Dimension Icon (300) microscope in Peak Force Tapping mode, employing antimony n-doped Si cantilevers (Bruker RTESPA-300) with a nominal resonant frequency of 300 kHz and a force constant of 40 N m^{-1}.

Cathodoluminescence: The CL was performed in a dedicated SEM with a parabolic mirror for light collection coupled to a monochromator. The emission was either detected by a photomultiplier tube for monochromatic imaging or a CCD for hyperspectral imaging. The SEM was equipped with a liquid helium cold stage (<10 K). The imaging was performed at 5 kV and a probe current of 10–50 pA. The monochromatic imaging was performed at 10 K and the hyperspectral imaging at room temperature.

Supporting Information

Supporting Information is available from the Wiley Online Library or from the author.

Acknowledgements

The authors would like to thank David Lindgren, Kristian Storm, and Rafal Ciechonski for their valuable inputs to this project. This research was performed at the Lund Nano Lab, a part of the MyFab facilities. The project was supported by the Swedish Research Council (VR), the Foundation for Strategic Research (SSF), the Knut and Alice Wallenberg Foundation (KAW), the Swedish Energy Agency, and Marie-Curie FP7-REA-GA 608153 (PhD4energy funding).

Conflict of Interest

The authors declare no conflict of interest.

Keywords

GaN, III-nitride, microprisms, photonics, self-assembly

Received: December 16, 2019
Revised: April 28, 2020
Published online: June 24, 2020

[1] A. C. Tamboli, E. D. Haberer, R. Sharma, K. H. Lee, S. Nakamura, E. L. Hu, *Nat. Photonics* **2007**, *1*, 61.
[2] H. Matsubara, S. Yoshimoto, H. Saito, Y. Jianglin, Y. Tanaka, S. Noda, *Science* **2008**, *319*, 445.
[3] H. Yoshida, Y. Yamashita, M. Kuwabara, H. Kan, *Nat. Photonics* **2008**, *2*, 551.
[4] T.-C. Lu, C.-C. Kao, H.-C. Kuo, G.-S. Huang, S.-C. Wang, *Appl. Phys. Lett.* **2008**, *92*, 141102.
[5] T. Wunderer, J. E. Northrup, Z. Yang, M. Teepe, A. Strittmatter, N. M. Johnson, P. Rotella, M. Wraback, *Appl. Phys. Lett.* **2011**, *99*, 201109.
[6] P. Bhattacharya, T. Frost, S. Deshpande, Md Z. Baten, A. Hazari, A. Das, *Phys. Rev. Lett.* **2014**, *112*, 236802.

[7] K. H. Li, X. Liu, Q. Wang, S. Zhao, Z. Mi, *Nat. Nanotechnol.* **2015**, *10*, 140.
[8] N. V. Triviño, R. Butté, J.-F. Carlin, N. Grandjean, *Nano Lett.* **2015**, *15*, 1259.
[9] Y. Sun, K. Zhou, Q. Sun, J. Liu, M. Feng, Z. Li, Y. Zhou, L. Zhang, D. Li, S. Zhang, M. Ikeda, S. Liu, H. Yang, *Nat. Photonics* **2016**, *10*, 595.
[10] T. Tao, T. Zhi, B. Liu, J. Dai, Z. Zhuang, Z. Xie, P. Chen, F. Ren, D. Chen, Y. Zheng, R. Zhang, *Adv. Funct. Mater.* **2017**, *27*, 1703198.
[11] Y.-B. Tang, X.-H. Bo, C.-S. Lee, H.-T. Cong, H.-M. Cheng, Z.-H. Chen, W.-J. Zhang, I. Bello, S.-T. Lee, *Adv. Funct. Mater.* **2008**, *18*, 3515.
[12] Q. Dai, M. F. Schubert, M. H. Kim, J. K. Kim, E. F. Schubert, D. D. Koleske, M. H. Crawford, S. R. Lee, A. J. Fischer, G. Thaler, M. A. Banas, *Appl. Phys. Lett.* **2009**, *94*, 111109.
[13] S. Tomiya, T. Hino, S. Goto, M. Takeya, M. Ikeda, *IEEE J. Sel. Top. Quantum Electron.* **2004**, *10*, 1277.
[14] M. Martens, F. Mehnke, C. Kuhn, C. Reich, V. Kueller, A. Knauer, C. Netzel, C. Hartmann, J. Wollweber, J. Rass, T. Wernicke, M. Bickermann, M. Weyers, M. Kneissl, *IEEE Photonics Technol. Lett.* **2014**, *26*, 342.
[15] P. Gibart, *Rep. Prog. Phys.* **2004**, *67*, 667.
[16] H. Lahrèche, P. Vennéguès, O. Tottereau, M. Laügt, P. Lorenzini, M. Leroux, B. Beaumont, P. Gibart, *J. Cryst. Growth* **2000**, *217*, 13.
[17] L. Liu, J. H. Edgar, *Mater. Sci. Eng., R* **2002**, *37*, 61.
[18] R. Yan, D. Gargas, P. Yang, *Nat. Photonics* **2009**, *3*, 569.
[19] T. Kuykendall, P. Ulrich, S. Aloni, P. Yang, *Nat. Mater.* **2007**, *6*, 951.
[20] Y.-T. Lin, T.-W. Yeh, Y. Nakajima, P. D Dapkus, *Adv. Funct. Mater.* **2014**, *24*, 3162.
[21] B. Monemar, B. J. Ohlsson, N. F. Gardner, L. Samuelson, in *Semiconductors and Semimetals*, Vol. *94*, Elsevier Inc., Amsterdam **2016**, pp. 227–271.
[22] S. D. Hersee, X. Sun, X. Wang, *Nano Lett.* **2006**, *6*, 1808.
[23] E. P. A. M. Bakkers, J. A. van Dam, S. De Franceschi, L. P. Kouwenhoven, M. Kaiser, M. Verheijen, H. Wondergem, P. van der Sluis, *Nat. Mater.* **2004**, *3*, 769.
[24] W. Guo, M. Zhang, A. Banerjee, P. Bhattacharya, *Nano Lett.* **2010**, *10*, 3356.
[25] S. Zhao, M. G. Kibria, Q. Wang, H. P. T. Nguyen, Z. Mi, *Nanoscale* **2013**, *5*, 5283.
[26] C. Hahn, Z. Zhang, A. Fu, C. H. Wu, Y. J. Hwang, D. J. Gargas, P. Yang, *ACS Nano* **2011**, *5*, 3970.
[27] P.-M. Coulon, B. Alloing, V. Brändli, P. Vennéguès, M. Leroux, J. Zúñiga-Pérez, *Appl. Phys. Express* **2016**, *9*, 015502.
[28] K. L. Kavanagh, *Semicond. Sci. Technol.* **2010**, *25*, 024006.
[29] Q. Sun, C. D. Yerino, B. Leung, J. Han, M. E. Coltrin, *J. Appl. Phys.* **2011**, *110*, 053517.
[30] B. N. Bryant, A. Hirai, E. C. Young, S. Nakamura, J. S. Speck, *J. Cryst. Growth* **2013**, *369*, 14.
[31] M. E. Coltrin, C. C. Mitchell, *J. Cryst. Growth* **2003**, *254*, 35.
[32] B. Leung, Q. Sun, C. D. Yerino, J. Han, M. E. Coltrin, *Semicond. Sci. Technol.* **2012**, *27*, 024005.
[33] V. Jindal, F. Shahedipour-Sandvik, *J. Appl. Phys.* **2009**, *106*, 083115.
[34] L. K. Aagesen, M. E. Coltrin, J. Han, K. Thornton, *J. Appl. Phys.* **2015**, *117*, 194302.
[35] A. T. M. Golam Sarwar, B. Leung, G. T. Wang, R. C. Myers, *Cryst. Growth Des.* **2018**, *18*, 1191.
[36] J. Colvin, R. Ciechonski, F. Lenrick, O. Hultin, M. Khalilian, A. Mikkelsen, A. Gustafsson, L. Samuelson, R. Timm, B. J Ohlsson, *Phys. Rev. Mater.* **2019**, *3*, 093604.
[37] J. C. Moore, J. E. Ortiz, J. Xie, H. Morkoç, A. A. Baski, *J. Phys.: Conf. Ser.* **2007**, *61*, 90.
[38] S. J. Rosner, E. C. Carr, M. J. Ludowise, G. Girolami, H. I. Erikson, *Appl. Phys. Lett.* **1997**, *70*, 420.
[39] G. Koblmüller, R. Averbeck, H. Riechert, P. Pongratz, *Phys. Rev. B* **2004**, *69*, 035325.
[40] J. E. Northrup, J. Neugebauer, R. M. Feenstra, A. R. Smith, *Phys. Rev. B* **2000**, *61*, 9932.
[41] U. W. Pohl, *Epitaxy of Semiconductors. Journal of Experimental Psychology: General*, Vol. *136*, Springer, Berlin **2013**.
[42] N. Pauc, M. R. Phillips, V. Aimez, D. Drouin, *Appl. Phys. Lett.* **2006**, *89*, 24.
[43] M. A. Reshchikov, H. Morkoç, *J. Appl. Phys.* **2005**, *97*, 061301.
[44] A. Gustafsson, *J. Microsc.* **2016**, *262*, 134.
[45] S. Meuret, T. Coenen, S. Y. Woo, Y.-H. Ra, Z. Mi, A. Polman, *Nano Lett.* **2018**, *18*, 2288.